Electrocatalysis

International Edition: DOI: 10.1002/anie.201812601
German Edition: DOI: 10.1002/ange.201812601

Amorphous Nanocages of Cu-Ni-Fe Hydr(oxy)oxide Prepared by Photocorrosion For Highly Efficient Oxygen Evolution

Zhi Cai, Lidong Li, Youwei Zhang, Zhao Yang, Jie Yang, Yingjie Guo, and Lin Guo**

Abstract: *Electrochemical water splitting requires efficient, low-cost water oxidation catalysts to accelerate the sluggish kinetics of the water oxidation reaction. A rapid photocorrosion method is now used to synthesize the homogeneous amorphous nanocages of Cu-Ni-Fe hydr(oxy)oxide as a highly efficient electrocatalyst for the oxygen evolution reaction (OER). The as-fabricated product exhibits a low overpotential of 224 mV on a glassy carbon electrode at 10 mA cm^{-2} (even lower down to 181 mV when supported on Ni foam) with a Tafel slope of 44 mV dec^{-1} for OER in an alkaline solution. The obtained catalyst shows an extraordinarily large mass activity of 1464.5 A g^{-1} at overpotential of 300 mV, which is the highest mass activity for OER. This synthetic strategy may open a brand new pathway to prepare copper-based ternary amorphous nanocages for greatly enhanced oxygen evolution.*

Electrochemical water splitting to produce hydrogen has been widely regarded as the most attractive approaches to obtain clean fuels from renewable energy sources. However, the efficiency of splitting water usually suffers from the sluggish kinetics of oxygen evolution reaction (OER),[1] which requires highly efficient and robust oxygen-evolving electrocatalysts to reduce the high overpotentials (η) and accelerate the reaction kinetics. The noble metal catalysts, such as Ir/Ru, have been identified as the most active OER electrocatalysts so far.[2] However, the high cost and the scarcity of such precious metals always limit their widespread use on scale-up development. Emerging as a family of outstanding alternatives, first-row transition metal (such as Ni, Co, Fe)-based catalysts, especially transition-metal oxides or (oxy)hydroxides, have attracted great attention, because of their remarkable catalytic activity, abundance, stability, and environmentally benign character.[3]

In particular, the nickel–iron (Ni-Fe)-based electrocatalysts exhibit superior performances for OER in alkaline solutions because of the strong synergistic effect by the incorporation of iron into nickel even in trace amounts.[4] Nocera and co-workers suggested that Fe^{3+} promotes the formation of the high-valence nickel ions, which in turn directly leads to enhanced OER activity.[5] Furthermore, the modification of Ni-Fe based catalysts are always attempted, such as improving the poor electronic conductivity by combining carbon materials.[6] Besides, Zhou and co-workers suggested the local electronic structure of Ni-Fe layered double hydroxide (LDH) could be modulated through interfacial interactions with FeOOH nanoparticles, which showed an excellent electrochemical activity.[7]

Apart from the synergistic effect and conductivity, amorphous structures with a large number of structural defects facilitate the diffusion and reaction of electrolyte ions. Also, the atomically homogeneously dispersed multi-transition-metal oxides or (oxy)hydroxides can alter the 3D electronic structure, thereby affecting the intrinsic activity of OER catalysts. Sargent and co-workers designed amorphous FeCoW oxyhydroxides with an atomically homogeneous metal distribution and proved that the coordination function of CoFeW can generate favorable electronic structure and enhance the energy of OER.[1a] Similar effects also occur in Cr, Ru added into NiFe-based catalysts.[8] However, the catalyst with low cost and high efficiency is still an ongoing challenge.

Herein, we first report homogenous amorphous nanocages of Cu-Ni-Fe hydr(oxy)oxide (AN-CuNiFe) as an extremely highly efficient OER electrocatalyst. The AN-CuNiFe was synthesized by a unique photocorrosion process with Cu_2O@amorphous nanocages of $NiFe(OH)_x$ (Cu_2O@AN-NiFe) as precursors. This electrocatalyst has exhibited remarkably high electrocatalytic activity for OER in an alkaline solution with an overpotential of 224 mV at a current density of 10 mA cm^{-2} with a Tafel slope of 44 mV dec^{-1} on glassy carbon (GC), The TOF value is as high as 3.3 s^{-1} at the overpotential of 300 mV. Of note, with a catalyst loading as low as 25 μg cm^{-2}, the AN-CuNiFe on GC obtained an extremely high mass activity of 1464.5 A g^{-1} at overpotential of 300 mV, which is 12.5 times higher than that of the state-of-art NiFe catalyst.[1a] To the best of our knowledge, it possesses the highest mass activity in basic media so far, indicating its outstanding intrinsic activity. Thus, we highly expect to explore a new pathway of lowering the overpotential by synthesizing copper-based amorphous hydroxide nanocages by a rapid photocorrosion process.

The synthesis route of AN-CuNiFe is illustrated in Figure 1 (I). Briefly, the whole synthesis process of AN-CuNiFe includes two steps. First, similar to our previous work,[9] Cu_2O@AN-NiFe core–shell precursor was synthesized by using a modified coordinating etching method via Cu_2O as a template (see details in the Supporting Information, Figures S1 and S2). Second, AN-CuNiFe were further synthesized by the photocorrosion method.

[*] Z. Cai, Prof. Dr. L. Li, Y. Zhang, Z. Yang, J. Yang, Y. Guo, Prof. Dr. L. Guo
Key Laboratory of Bio-Inspired Smart Interfacial Science and Technology of Ministry of Education, Beijing Advanced Innovation Center for Biomedical Engineering, School of Chemistry
Beihang University, Beijing, 100191 (P. R. China)
E-mail: lilidong@buaa.edu.cn
guolin@buaa.edu.cn

Supporting information and the ORCID identification number(s) for the author(s) of this article can be found under: https://doi.org/10.1002/anie.201812601.

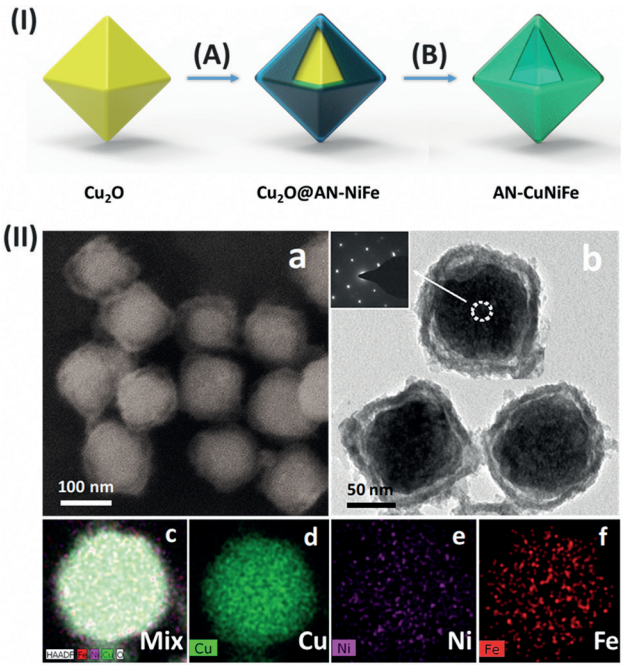

Figure 1. I) Representation of the synthesis route of AN-CuNiFe. A) Coordinating etching process, B) photocorrosion process. II) Morphology characterizations of Cu_2O@AN-NiFe precursor. a) SEM image and b) TEM image with SAED pattern inserted, and c)–f) EDS elemental mapping images for Cu, Ni, and Fe elements of the Cu_2O@AN-NiFe precursor.

As illustrated in Figure 1(II)a, the scanning electron microscopy (SEM) image shows that the geometrics and dimensions of the precursor sample are basically the same as the Cu_2O templates with a uniform diameter of about 100 nm. The transmission electron microscope (TEM) image in Figure 1b shows the core–shell structure of the precursor. The shell surface is rather rough, which is as thin as about 10 nm. The inset of Figure 1b shows the selected-area electron-diffraction (SAED) pattern of the precursor, indicating the crystal nature of Cu_2O core. It suggests the shell might have an amorphous nature, which can be supported by the only observation of Cu_2O diffraction peaks in the X-ray diffraction (XRD) pattern as shown in the Supporting Information, Figure S3. To confirm this assumption, an excessive amount of $Na_2S_2O_3$ was added, then the cuprous oxide was completely etched and only Ni-Fe double hydroxides were left. Based on the TEM image, SAED pattern, and X-ray photoelectron spectroscopy (XPS) in the Supporting Information, Figure S4, the eventually formed nanocages of Ni-Fe hydroxides are in amorphous state, so we call it amorphous nanocages of Ni-Fe (AN-NiFe). Furthermore, as shown in Figure 1c–f, the signals of elements Cu, Fe, Ni, are clearly observed, respectively, suggesting that amorphous Ni-Fe double hydroxides cover the Cu_2O surface uniformly.

Next, we produced AN-CuNiFe by a photocorrosion process. The photocorrosion of Cu_2O will occur in an alkaline solution under light illumination, which usually causes poor photo-electrochemical catalytic performance of pure Cu_2O.[10] Interestingly, in this work, we use this photocorrosion reaction to introduce Cu into AN-NiFe shell by light illumination, and enhance the facial electron transfer during catalytic process. In detail, the AN-CuNiFe was obtained from the Cu_2O@AN-NiFe by using 20 linear sweep voltammetry (LSV) scans from 0.2 V to 0.6 V vs. Ag/AgCl with a sweep rate of 50 $mV s^{-1}$ in 1 M KOH solution under AM 1.5 G illumination. As shown in Figure 2a, the nanocages

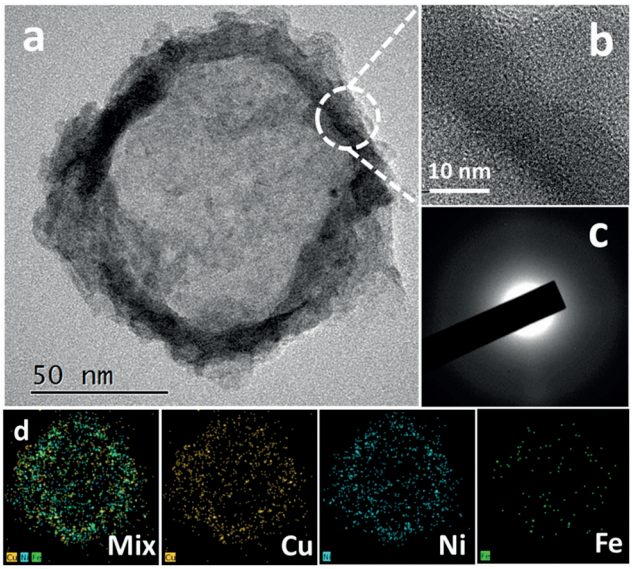

Figure 2. a) TEM image, b) HRTEM image, c) SAED pattern, and d) EDS elemental mapping images for Cu, Ni, and Fe elements of AN-CuNiFe.

with 10 nm thickness were obtained from the core–shell precursor after this photocorrosion process. The high-resolution TEM image of AN-CuNiFe (Figure 2b) and the corresponding fast Fourier transform (FFT) image in short range (Supporting Information, Figure S5) show it is of an amorphous state. The corresponding SAED patterns of nanocages (Figure 2c) also suggest that the AN-CuNiFe are amorphous, which is also proved by XRD pattern in the Supporting Information, Figure S6. Of note, the whole Cu_2O core has completely disappeared. The EDS mapping shows that copper has been evenly distributed into AN-NiFe shell, and uniformly mixed with the amorphous structure of the $NiFe(OH)_x$ shell to form a new ternary amorphous nanocages of Cu-Ni-Fe hydr(oxy)oxide with an atomically homogeneous metal distribution (as shown in Figure 2d). The EDS spectrum of the sample (Supporting Information, Figure S7) shows the presence of Cu, Ni and Fe elements with an atomic molar ratio of 10:8:1.

The chemical state of AN-CuNiFe catalyst was studied by the X-ray photoelectron spectroscopy (XPS; more details, see the Supporting Information, Figure S8). In the XPS spectra, Cu, Ni, Fe, and O are observed in the XPS spectrum, suggesting that a trimetallic composite is obtained. Ni shows a distinct Ni $2p_{1/2}$ peak and $2p_{3/2}$ peak around 874 and 856 eV, respectively, along with a strong satellite peak indicating the presence of $Ni^{2+/3+}$. The main Cu $2p_{3/2}$ peak (934.1 eV) with a strong satellite can be uniquely attributed to Cu^{2+}. Fe^{3+} can

be recognized by a fairly broad Fe $2p_{3/2}$ peak around 712 eV along with a small but significant satellite near 718 eV. Meanwhile, Fe 3p XPS was also conducted, the peak at circa 56.2 eV also confirms the Fe is mostly in Fe^{3+} oxidation state in the AN-CuNiFe (Supporting Information, Figure S9). The main O peak component is at 530.5 eV and 531.6 eV, which is assigned to oxygen in the form of O_2^{2-}/O^- and the hydroxyl groups (−OH) on the surface, respectively. This can be attributed to the O of metal oxide and hydroxide.

To investigate the photocorrosion process from Cu_2O@AN-NiFe to AN-CuNiFe, TEM and electrochemical tests of different LSV scans (3rd, 10th, 20th) under AM 1.5 G illumination were carried out. As shown in the Supporting Information, Figure S10, with the color of catalysts change from yellow to black, the core–shell structure turns to nanocages, during which process, Cu_2O core was totally corroded (Supporting Information, Figure S10 a,c,e). After 20 scans, the core is completely dissolved, leaching into the shell of NiFe hydroxide structure to form an evenly distributed CuNiFe amorphous phase. During the scans, the core of catalyst disappears gradually (Supporting Information, Figure S10 c) and the perfection of the crystal became lower with disorder brightened dots in the SAED pattern as shown in the Supporting Information, Figure S10 d. Correspondingly, the LSV curves kept rising during the scanning process until 20th scan, then became stable. It suggests that the catalyst has completely changed after photocorrosion process (Supporting Information, Figure S11).

To further study the photocorrosion mechanism, Cu_2O@AN-NiFe precursors were scanned under the same conditions on GC electrode without light illumination. The TEM and EDS elemental mapping image showed that the Cu_2O core did not be corroded, and the core–shell structure still maintained after 20 LSV scans in dark (Supporting Information, Figure S12), which confirms light is a key factor for the synthesis of AN-CuNiFe. Of note, Cu_2O@AN-NiFe also experienced the electro-activation process without light illumination, which generally exists in OER of nickel–iron catalysts.[11] By comparison (Supporting Information, Figure S13), we found that the catalyst after electro-activation is quite different from the AN-CuNiFe obtained from the photocorrosion process. Additionally, a high pH environment is another key factor to help the dissolution of Cu_2O core. The TEM image of the product after 20 LSV scans under light, but in 0.01 M KOH (pH 12), are shown in the Supporting Information, Figure S14. It can be clearly seen that the core–shell structure still maintains, indicating Cu_2O core cannot be dissolved with lower pH environment, which can be further proved by the results as shown in the Supporting Information, Figure S15. The above results indicate that this photocorrosion process can only take place in strong basic media under light.

As the light traveled through the 10 nm layer of AN-NiFe shell, the photogenerated electrons and holes were produced on Cu_2O. As depicted in the Supporting Information, Scheme S1 [Eqs. (1)–(3)], the photogenerated electrons and holes can rouse a series of reactions as follows:[10] Firstly, the photo-generated electrons will flow into the Ni-foam substrate electrode with the assistance of external positive potential, which helps the fast separation of electron and holes. Secondly, photogenerated holes can oxidize Cu_2O to CuO [Eq. (2)]. Afterwards, CuO can react with extra OH^- to dissolve into $[Cu(OH)_4]^{2-}$ and then diffuse into the amorphous shell structure of $NiFe(OH)_x$. Owing to the continuous depletion of OH^- at the interface between catalyst and electrolyte for the oxygen evolution reaction, the pH is relatively lower on the shell. Thus, $[Cu(OH)_4]^{2-}$ will loose OH^- to precipitate as $Cu(OH)_2$ [Eq. (4)], then evenly distributed into the shell and form a AN-CuNiFe. Thus, Cu_2O can be photocorroded and incorporated into the amorphous shell to form AN-CuNiFe in the strong alkaline solution.

To evaluate the catalytic activities of as-prepared AN-CuNiFe, the electrochemical measurements for OER on GC electrode in KOH solution (pH 14) were carried out (Figure 3). To compare OER performance with AN-CuNiFe, the state-of-the-art NiFe LDH catalyst was prepared by using previous method.[12] Figure 3 a shows the linear sweep voltammetry (LSV) curves (no *iR* correction) of all samples at a scan rate of 10 mV s^{-1}. Tafel slopes were used to verify that the reaction kinetics of AN-CuNiFe (Figure 3 b). The polarization curve of the AN-CuNiFe shows excellent OER activity with overpotential of 224 mV at 10 mA cm^{-2}

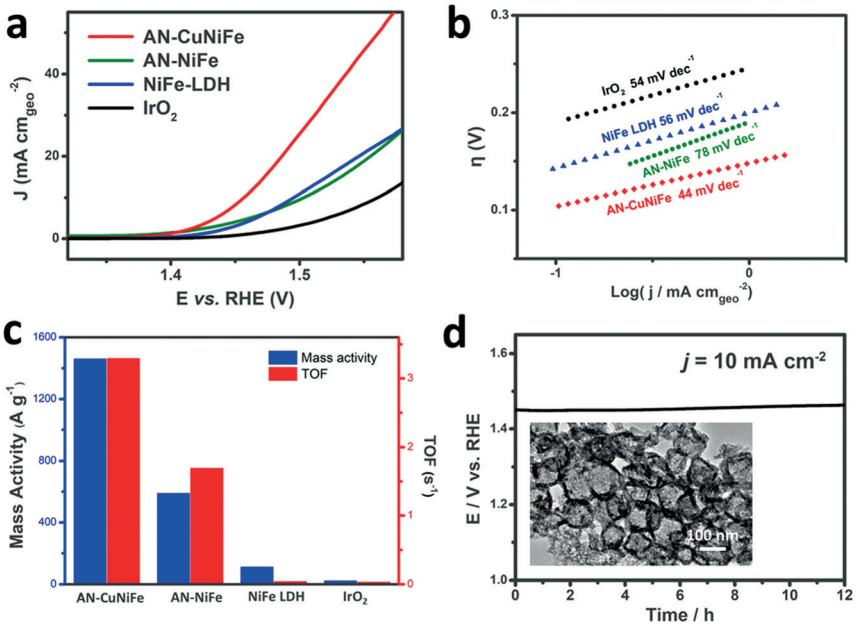

Figure 3. a) Polarization curves b) Tafel plots and c) Mass activity and TOF comparison of AN-CuNiFe, AN-NiFe, NiFe LDH and IrO_2 in 1 M KOH solution on glassy carbon electrode, d) Chronopotentiometry of AN-CuNiFe at a current density of 10 mA cm^{-2} with TEM image of the AN-CuNiFe sample after 12 h in-dark test inserted, scale bar is 100 nm.

and a Tafel slope of 44 mV dec^{-1} on GC electrode. The overpotential (η) is 42, 46, and 106 mV lower than that of NiFe LDH, AN-NiFe, and IrO_2, respectively. Especially, the mass activity of AN-CuNiFe is 1464.5 A g^{-1} at overpotential of 0.3 V with a very low catalyst loading mass of 0.025 mg cm^{-2}, which is about 2.5 times higher than that of AN-NiFe and 12.5 times higher than that of the state-of-the-art NiFe catalyst (Figure 3c; Supporting Information, Table S1). To the best of our knowledge, it possesses the highest mass activity reported to date, indicating its outstanding intrinsic electrocatalytic activity.

Moreover, taking account of the surface area, the specific activity (j_{ECSA}) was also used to compare OER intrinsic activity of catalysts (more details in the Supporting Information, Table S2 and Figure S16). The results show that AN-CuNiFe provide the highest j_{ECSA}, further reflecting its excellent intrinsic activity. Meanwhile, the intrinsic OER catalytic activities of AN-CuNiFe and AN-NiFe can also be evaluated by calculating the turnover frequency (TOF) assuming that all the Cu, Ni and Fe sites are involved in OER. The TOF associated with AN-CuNiFe at the overpotential of 300 mV is 3.3 s^{-1}, which is almost two-fold higher than that obtained with AN-NiFe (1.7 s^{-1}). The plot from the chronopotentiometry (CP) test in Figure 3d also shows the AN-CuNiFe performs excellent stability with potential remaining at about 1.45 V at 10 mA cm^{-2} for 12 h in-dark test in alkaline electrolyte (Figure 3d). Also, the LSV curve of AN-CuNiFe remains the same after 500 scans (Supporting Information, Figure S17). Of note, the inserted TEM image shows unchanged morphology of the amorphous nanocages with scale bar of 100 nm after a 12 hour test, disclosing their structural stability.

Furthermore, the comparison of LSV performance of AN-CuNiFe with AN-CuNi and AN-CuFe was also analyzed (Supporting Information, Figure S18). The results show that AN-CuNiFe has the best electrochemical performance compared with binary elements owing to the synergistic effect. Electrochemical impedance spectroscopy (EIS) was employed to investigate the charge transfer abilities. The semicircle of Nyquist plot at the high-frequency region represents the charge transfer resistance (R_{ct}) from the mass transfer during electrocatalytic reaction. In agreement with our original design, we find that the electrical conductivity of the catalyst has been remarkably improved with the incorporation of Cu ions into the shell structure (Supporting Information, Figure S19).

We also tested the electrocatalytic activity of AN-CuNiFe on more conductive electrode substrate of nickel foam with much larger surface area for comparision. As shown in the Supporting Information, Figure S20, AN-CuNiFe exhibits remarkable OER activity with even lower overpotential of 181 mV at 10 mA cm^{-2} and a Tafel slope of 34 mV dec^{-1} on a Ni foam electrode. Similarly, to compare the intrinsic activity, C_{dl}, roughness factor (RF), and j_{ECSA} were also evaluated (Supporting Information, Figure S21 and Table S3). The results show that the trend of electrochemical performance on Ni foam is consistent with that on GC electrode.

Previous work reported that high-valence Ni promotes the energy band of O near the Fermi surface, thus realizing the activation of lattice O sites and enhancing the activity of OER.[11] That is, the in situ oxidation of $Ni(OH)_2$ (Ni^{II}) to NiOOH ($Ni^{III/IV}$) is particularly important to facilitate OER. Herein, the great enhancement of AN-CuNiFe performance over AN-NiFe inspires us that the introduction of Cu might be essentially related to the increasing extent of $Ni^{II}/Ni^{III/IV}$ transformation. As shown in Figure 4, a detailed fitting of XPS reveals that a Ni^{3+}/Ni^{2+} ratio of 1.4:1 at the beginning of photocorrosion increases to 3.0:1 in the middle and finally reaches up to 3.9:1 at the end. Meanwhile, a ratio of O2 (corresponding to the O in NiOOH) to O3 (corresponding to the O in $Ni(OH)_2$) increases from 0.59:1 at the beginning to 0.75:1 in the middle, eventually up to 1.25:1 after the photocorrosion. In contrast, the oxidation state of Fe element does not change obviously during the photocorrosion process (Supporting Information, Figure S22). Both XPS results of Ni 2p and O 1s indicate that more Ni^{2+} has been oxidized to Ni^{3+} during the photocorrosion process, leading to a higher content of NiOOH active species in the composite, which

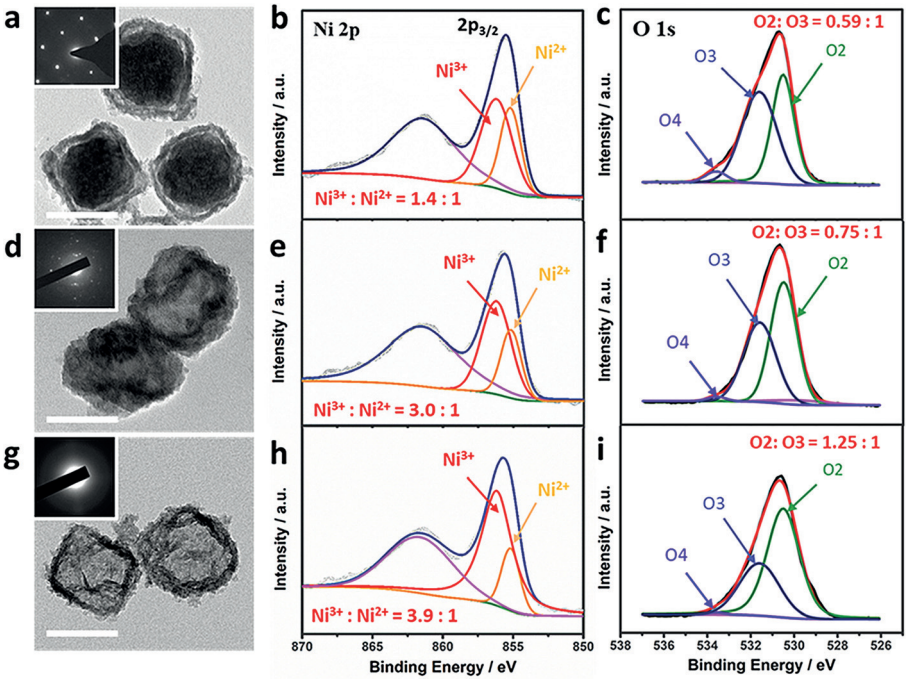

Figure 4. Characterizations of photocorrosion process. TEM images and Ni 2p, O 1s XPS spectra of the Cu_2O@AN-NiFe precursor with the corresponding SAED pattern inserted a)–c) obtained after first LSV scan, d)–f) obtained after 10th LSV scans, and g)–i) obtained after 20th LSV scans under light illumination (AN-CuNiFe). Scale bars of TEM images: 100 nm.

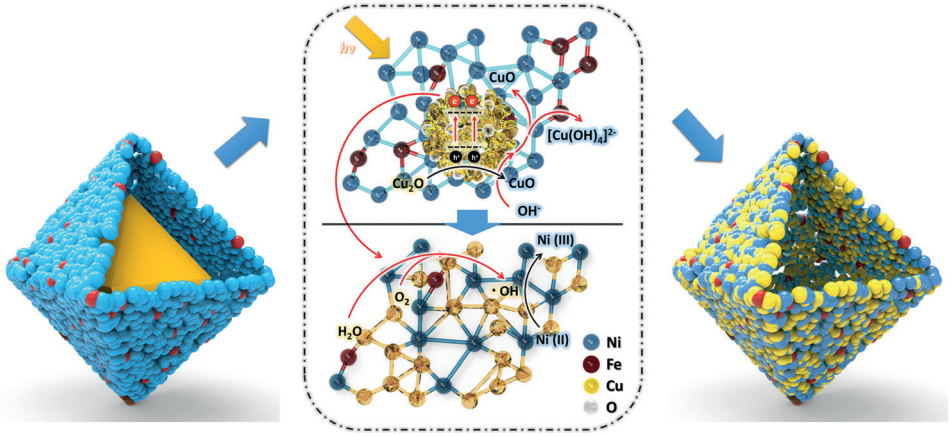

Figure 5. Schematic illustration of OER catalysis enhancement mechanism.

gives rise to the greatly enhanced OER activity. The fact that the introduction of Cu increases the amount of $Ni^{III/IV}$ can be explained by the photocorrosion mechanism.[10a] As shown in Figure 5, the photo-generated electrons can be scavenged by molecular oxygen O_2 to yield $O_2^{-\cdot}$ or H_2O_2 and OH^-. Afterwards, $O_2^{-\cdot}$ and H_2O_2 can further interreact to produce O_2 and ·OH. It is well known that the ·OH is a very powerful oxidizing agent with a redox potential of +1.9 V, which can oxidize Ni^{2+} to Ni^{3+} for later OER reaction (details are shown in the Supporting Information, Scheme S1, Eqs. (5)–(13)]. To confirm the above speculation, coumarin, as an effective ·OH trapper, was added into our system, OER activity significantly decreased as shown in Figure S23 (more details are also shown in the Supporting Information).

Above all, we propose the following four points to explain the observed great enhancements in OER electrocatalytical activity. First, as shown in Figure 5 and the Supporting Information, Scheme S1, Equations (5)–(13), under light irradiation and high pH condition, the photocorroded Cu_2O produce a large amount of ·OH, which act as effective electron trappers to capture electrons from $Ni(OH)_2$, significantly increase the amount of $Ni^{III/IV}$ active species in the amorphous shell. Such intrinsic charge transfer can be confirmed by XPS results (Figure 4). Second, the amorphous nanocage structure of catalysts provide more active spots and high intrinsic activity of OER, which can be supported by the highest mass activity, j_{ECSA}, TOF values of AN-CuNiFe. Third, the incorporation of Cu to form AN-CuNiFe hydr(oxy)oxide significantly reduce the Faraday impedance of the catalyst as confirmed by previous EIS results (Supporting Information, Figure S19). This greatly compensated for the poor conductivity of amorphous materials. Fourth, the 3d electronic structure and energetics of OER intermediates can be modulated by homogeneously dispersed incorporating Cu elements, which is a synergistic effect arises between Ni and Fe/Cu.[13] It suggests a partial charge transfer between Ni and Fe/Cu centers, which can be attributed to the high electronegativity of Fe^{3+}/Cu^{2+}. Therefore, the Ni active site becomes more electropositive and exhibits a stronger attraction towards the OH^- species, which is helpful to promote the catalytic activity.

In conclusion, by using core–shell Cu_2O@AN-NiFe as precursors, we first synthesized amorphous nanocages of Cu-Ni-Fe hydr(oxy)oxides via a rapid photocorrosion process. As an OER catalyst, it shows the excellent overpotential of 224 mV at 10 mA cm^{-2} with a Tafel slope of 44 mV dec^{-1}. In particular, the obtained AN-CuNiFe shows an extremely large mass activity of 1464.5 A g^{-1} on GC at overpotential of 300 mV, which is the highest mass activity up to date. This outstanding catalytic performance is attributed to the enhanced generation of $Ni^{(III/IV)}$ active species and improved charge transfer with the introduction of Cu into the AN-NiFe. These findings highlight the possibility of activating OER catalysis by photocorrosion and could open new avenues toward the synthesis design of copper-based ternary amorphous nanocage catalysts.

Acknowledgements

Funding: This work was financially supported by National Natural Science Foundation of China (no. 51532001 and 51872016).

Conflict of interest

The authors declare no conflict of interest.

Keywords: amorphous materials · mass activity · nanocages · oxygen evolution reaction · ternary CuNiFe

How to cite: *Angew. Chem. Int. Ed.* **2019**, *58*, 4189–4194
Angew. Chem. **2019**, *131*, 4233–4238

[1] a) B. Zhang, X. Zheng, O. Voznyy, R. Comin, M. Bajdich, M. Garcia-Melchor, L. Han, J. Xu, M. Liu, L. Zheng, F. P. G. de Arquer, C. T. Dinh, F. Fan, M. Yuan, E. Yassitepe, N. Chen, T. Regier, P. Liu, Y. Li, P. De Luna, A. Janmohamed, H. Xin, H. Yang, A. Vojvodic, E. H. Sargent, *Science* **2016**, *352*, 333–337; b) M. W. Kanan, D. G. Nocera, *Science* **2008**, *321*, 1072–1075.
[2] Y. Lee, J. Suntivich, K. J. May, E. E. Perry, Y. Shao-Horn, *J. Phys. Chem. Lett.* **2012**, *3*, 399–404.
[3] a) M. Gong, H. Dai, *Nano Res.* **2015**, *8*, 23–39; b) X. Lu, C. A. Zhao, *Nat. Commun.* **2015**, *6*, 6616; c) K. Fan, H. Chen, Y. Ji, H. Huang, P. M. Claesson, Q. Daniel, B. Philippe, H. Rensmo, F. Li, Y. Luo, L. Sun, *Nat. Commun.* **2016**, *7*, 11981; d) M. S. Burke, M. G. Kast, L. Trotochaud, A. M. Smith, S. W. Boettcher, *J. Am. Chem. Soc.* **2015**, *137*, 3638–3648; e) P. Zhang, L. Li, D. Nordlund, H. Chen, L. Fan, B. Zhang, X. Sheng, Q. Daniel, L. Sun, *Nat. Commun.* **2018**, *9*, 381; f) J. Nai, Y. Lu, L. Yu, X. Wang, X. Lou, *Adv. Mater.* **2017**, *29*, 1703870.

[4] M. B. Stevens, T. Cdm, L. J. Enman, J. Deng, S. W. Boettcher, *J. Am. Chem. Soc.* **2017**, *139*, 11361 – 11364.
[5] N. Li, D. K. Bediako, R. G. Hadt, D. Hayes, T. J. Kempa, F. von Cube, D. C. Bell, L. X. Chen, D. G. Nocera, *Proc. Natl. Acad. Sci. USA* **2017**, *114*, 1486 – 1491.
[6] a) W. Ma, R. Z. Ma, C. Wang, J. Liang, X. Liu, K. Zhou, T. Sasaki, *ACS Nano* **2015**, *9*, 1977 – 1984; b) M. Gong, Y. Li, H. Wang, Y. Liang, J. Wu, J. Zhou, J. Wang, T. Regier, F. Wei, H. Dai, *J. Am. Chem. Soc.* **2013**, *135*, 8452 – 8455.
[7] J. Chen, F. Zheng, S. Zhang, A. Fisher, Y. Zhou, Z. Wang, Y. Li, B. Xu, J. Li, S. Sun, *ACS Catal.* **2018**, *8*, 11342 – 11351.
[8] a) Y. Yang, L. Dang, M. J. Shearer, H. Sheng, W. Li, J. Chen, P. Xiao, Y. Zhang, R. J. Hamers, S. Jin, *Adv. Energy Mater.* **2018**, *8*, 1703189; b) G. Chen, T. Wang, J. Zhang, P. Liu, H. Sun, X. Zhuang, M. Chen, X. Feng, *Adv. Mater.* **2018**, *30*, 1706279.
[9] J. Nai, H. Yin, T. You, L. Zheng, J. Zhang, P. Wang, Z. Jin, Y. Tian, J. Liu, Z. Tang, L. Guo, *Adv. Energy Mater.* **2015**, *5*, 1614 – 6832.
[10] a) L. Huang, F. Peng, H. Yu, H. Wang, *Solid State Sci.* **2009**, *11*, 129 – 138; b) C. Y. Toe, Z. Zheng, H. Wu, J. Scott, R. Amal, Y. H. Ng, *Angew. Chem. Int. Ed.* **2018**, *57*, 13613 – 13617; *Angew. Chem.* **2018**, *130*, 13801 – 13805.
[11] X. Su, Y. Wang, J. Zhou, S. Gu, J. Li, S. Zhang, *J. Am. Chem. Soc.* **2018**, *140*, 11286 – 11292.
[12] Z. Li, M. Shao, H. An, Z. Wang, S. Xu, M. Wei, D. Evans, X. Duan, *Chem. Sci.* **2015**, *6*, 6624 – 6631.
[13] a) L. Trotochaud, S. L. Young, J. K. Ranney, S. W. Boettcher, *J. Am. Chem. Soc.* **2014**, *136*, 6744 – 6753; b) M. W. Louie, A. T. Bell, *J. Am. Chem. Soc.* **2013**, *135*, 12329; c) Y. Xiaowen, M. Zhang, W. Yuan, G. Shi, *J. Mater. Chem. A* **2015**, *3*, 6921 – 6928.

Manuscript received: November 9, 2018
Revised manuscript received: December 13, 2018
Accepted manuscript online: January 22, 2019
Version of record online: February 25, 2019

